Journal of Structural Geology 32 (2010) 1334–1348

Contents lists available at ScienceDirect

Journal of Structural Geology

journal homepage: www.elsevier.com/locate/jsg

Fault zone structure and fluid–rock interaction of a high angle normal fault in Carrara marble (NW Tuscany, Italy)

G. Molli [a,*], G. Cortecci [b], L. Vaselli [b], G. Ottria [b], A. Cortopassi [c], E. Dinelli [d], M. Mussi [b], M. Barbieri [e]

[a] Dipartimento di Scienze della Terra, Università di Pisa, Via S. Maria 53, I-56126 Pisa, Italy
[b] CNR Istituto di Geoscienze e Georisorse Pisa, Italy
[c] Azienda U.S.L. n°1 Massa-Carrara, Unità operativa Ingegneria Mineraria, Italy
[d] Centro di Ricerca Interdipartimentale per le Scienze Ambientali, Università di Bologna, Ravenna, Italy
[e] Dipartimento di Scienze della Terra, Università "La Sapienza", Roma, Italy

ARTICLE INFO

Article history:
Received 20 March 2008
Received in revised form
21 April 2009
Accepted 27 April 2009
Available online 21 May 2009

Keywords:
Fault zone architecture
Carrara marble
Microstructures
Fault rocks
Fluid–rock interactions
Alpi Apuane

ABSTRACT

We studied the geometry, intensity of deformation and fluid–rock interaction of a high angle normal fault within Carrara marble in the Alpi Apuane NW Tuscany, Italy. The fault is comprised of a core bounded by two major, non-parallel slip surfaces. The fault core, marked by crush breccia and cataclasites, asymmetrically grades to the host protolith through a damage zone, which is well developed only in the footwall block. On the contrary, the transition from the fault core to the hangingwall protolith is sharply defined by the upper main slip surface. Faulting was associated with fluid–rock interaction, as evidenced by kinematically related veins observable in the damage zone and fluid channelling within the fault core, where an orange–brownish cataclasite matrix can be observed. A chemical and isotopic study of veins and different structural elements of the fault zone (protolith, damage zone and fault core), including a mathematical model, was performed to document type, role, and activity of fluid–rock interactions during deformation. The results of our studies suggested that deformation pattern was mainly controlled by processes associated with a linking-damage zone at a fault tip, development of a fault core, localization and channelling of fluids within the fault zone. Syn-kinematic microstructural modification of calcite microfabric possibly played a role in confining fluid percolation.

1. Introduction

Fault growth processes commonly produce a fault zone architecture comprising a fault core, bounded by slip surfaces, including comminuted and fragmented rock material and a volume of distributed deformation surrounding the core denoted as damage zone (e.g. Chester and Logan, 1986; Knipe and Lloyd, 1994; McGrath and Davison, 1995; Caine et al., 1996; Cello et al., 2001a,b; Storti et al., 2003; Billi et al., 2003; Kim et al., 2004; Agosta and Aydin, 2006). The fault core represents the part of a fault zone in which most of the displacement was accommodated (Caine et al., 1996), whereas the damage zone, which includes fault-related subsidiary structures can be associated with distributed deformation developed during the different stages (pre-faulting, fault propagation, displacement and linkage) of fault zone growth (e.g. Chester and Logan, 1986; Peacock, 2002; Faulkner et al., 2003).

Kim et al. (2004) divided the fault damage zone into three types, namely: tip-, linking- and wall damage zones based on position within and around the fault zone itself. Although physical models of fault growth address the complexity of fault propagation (e.g. Vermilye and Scholz, 1998; Peacock, 2002 and references), actual three-dimensional damage zone geometry should be considered to understand the slip mode and evolutionary stages of a given zone.

Inclined faults commonly show an asymmetric strain pattern around the fault core which justifies the proposed separation of the damage zone into distinct footwall- and hangingwall damage domains (Berg and Skar, 2005). The asymmetric deformation pattern has been related (e.g. Mandl, 2000; Flodin and Aydin, 2004; Berg and Skar, 2005 and references therein) to: i) geometric controls (e.g. irregularity of fault trace); ii) differences in stress conditions during faulting; iii) differences in rock properties across the fault; iiii) growth process of the fault zone.

Fault zones may have important control on subsurface fluid flow (McCaig, 1988; Sibson, 1992, 1996; Antonellini and Aydin, 1994), acting as localized conduits, barriers and (or) combined conduit-barrier (e.g. Knipe, 1993; Caine et al., 1996; Kirschner and Kennedy, 2001; Rawling et al., 2001; Cello et al., 2001a,b; Storti et al., 2003;

* Corresponding author. Tel.: +39 050 2215749.
E-mail address: gmolli@dst.unipi.it (G. Molli).

0191-8141/$ – see front matter © 2009 Elsevier Ltd. All rights reserved.
doi:10.1016/j.jsg.2009.04.021

Micarelli et al., 2006) because permeability may be several orders of magnitude different from the host rock (Evans et al., 1997; Caine and Forster, 1999; Agosta et al., 2007). Moreover, fluids channelized within fault zones strongly influence the rheological behaviour and the dynamics of faulting (e.g. Brodie and Rutter, 1985; Marquer and Burkhard, 1992; Bruhn et al., 1994; Sibson, 1992, 1996; Schultz and Evans, 1998; Faulkner and Rutter, 2001; Kennedy and White, 2001; Labaume et al., 2004; Micklethwaite and Cox, 2004; Mancktelow and Pennacchioni, 2005; Miller et al., 2008).

In this contribution we present the results of a structural investigation of a high angle normal fault developed in the Alpi Apuane (NW Tuscany, Italy). The fault studied, hosted within Jurassic marbles (the well known Carrara marbles), gives us the opportunity to compare and infer natural fault zone formation products and process with those developed in experimental deformation of the same material under controlled physical conditions (P, T, strain rate and fluids) (e.g. Rutter, 1972; Schmid et al., 1980; Fredrich et al., 1989; Burlini and Bruhn, 2005; Han et al., 2007). Moreover, the suitability of the described models for an asymmetric strain distribution within a homogeneous coarse grained carbonate protolith can be examinated.

2. Geological setting

The Alpi Apuane, in which the studied structure is hosted, expose the deepest structural level of the northern Apennine nappe stack (Fig. 1). The rock units represent the distal part of the Adria continental margin (Tuscan Domain), lying below the westerly derived oceanic Ligurian and sub-Ligurian accretionary wedge units (Elter, 1975; Carmignani and Kligfield, 1990; Carmignani et al., 2000; Molli, 2008). The lithostratigraphic sequence exposed in the Alpi Apuane is made up of a Paleozoic basement unconformably overlain by an Upper Triassic–Oligocene metasedimentary sequence. The Mesozoic cover-rocks include thin Triassic continental to shallow water Verrucano-like deposits, followed by Upper Triassic–Liassic carbonate platform metasediments comprising dolostones (“Grezzoni”), dolomitic marbles and marbles (the “Carrara marbles”), and then by Upper Liassic–Lower Cretaceous cherty metalimestone, cherts and calcschists. Lower Cretaceous to Lower Oligocene sericitic phyllites and calcschists, with marble interlayers, were deposited in deep water during drowning of the former carbonate platform. The Oligocene deposition of turbiditic sandstones (Pseudomacigno formation) closed the sedimentary history of the continental margin.

The Tertiary tectonic evolution of the Alpi Apuane includes an early stage of deep underthrusting associated with peak metamorphism (temperature of 350–450 °C; pressure of 0.5–0.6 GPa) and isoclinal folding. This was followed by deformation associated with syn-contractional exhumation, during which folding and subhorizontal crenulation cleavage was developed (Molli and Vaselli, 2006; Meccheri et al., 2007; Molli, 2008). The latest stages of geological evolution, associated with the final exhumation and uplift of the Alpi Apuane, were characterized by brittle faulting (low angle and high angle faults) during “post-orogenic” regional extension of the inner part of the Northern Apennine wedge (Carmignani and Kligfield, 1990; Patacca et al., 1992; Ottria and Molli, 2000; Molli, 2008).

In terms of brittle deformation, the Alpi Apuane represents (Fig. 1) a homogeneous domain of “low strain” surrounded, both to the east and to the west, by main faults (border faults) which separate the Alpi Apuane from the seismically active tectonic depressions of lower Lunigiana/Versilia, to the west, and Garfagnana to the east (Carmignani et al., 2000; Molli, 2008). Within the Alpi Apuane, the brittle structures formed during a protracted history of deformation in which an initially mutually interfering system of strike-slip and normal faulting was followed by the development of normal faults (Ottria and Molli, 2000). Available thermochronometric studies (Abbate et al., 1994; Balestrieri et al., 2003), in particular those more recently performed including (U–Th)/He and fission-track ages on zircon and apatite (Fellin et al., 2007), allow to constrain the stages of high angle faulting within the last 5 Ma, during which 3–4 km of rock uplift occurred.

3. Mesostructural and microstructural data

The analyzed fault, exposed in the central part of the Carrara marble basin, is observed across artificial exposures of an underground quarry in the Fantiscritti marble basin (Fig. 2).

In this area, the tectonically derived mechanical multilayer produced by isoclinal folding of the original stratigraphic sequence is formed by a “homogeneous” massive marble layer of, at least, 600 m in thickness, overlaying dolomitic marbles and dolomites (Marmi Dolomitici and Grezzoni fms.) and the pre-Mesozoic basement. These latter units are exposed about 2 km east of the study area where they dip westward toward it. The depth of the contact between pre-Mesozoic basement and overlying units (Fig. 2) cannot be precisely defined, but it can be geometrically estimated as being 400–500 m vertically beneath the structure. The fault zone studied can be observed for 25 m along strike and for about 40 m in direction normal to it. In the geological map in Fig. 2, the fault was drawn by tracing the structure up-dip for about 200 m to intercept the surface and by subsequent control through direct observations.

The data used in this study were obtained directly from outcrops analysis by using conventional structural techniques, digital imaging, fracture trace mapping, and scan-line methods. The performed scan lines were from 10 m to 35 m long, oriented along horizontal and vertical outcrops of the quarry. Traverses perpendicular and/or oblique to the fault zone were also accomplished.

The analyzed fault zone is represented in Figs. 3 and 4. For each fault-related structure the following parameters were observed and recorded along a scan line (e.g. Knott et al., 1996; Cello et al., 2001a; Caine and Tomusiak, 2003): (i) type of discontinuities (e.g. fractures vs. veins), (ii) spatial position, (ii) attitude (angle of dip and dip direction), (iii) width, (iv) morphology of discontinuity surface, with additional parameters represented by (v) type of fault rocks (in the fault core), (vi) azimuth and angle of plunge of striae (if present), (vii) sense of displacement (if available).

From this analysis, the mean orientation of the discontinuities associated with the fault zone was obtained, allowing a semi-quantitative assessment of the overall architecture and related potential permeability anisotropy of the fault zone. This was done using the architectural indices of Caine et al. (1996) to assess the conduit/barrier properties of the fault zone which were deciphered on the basis of relative varying thickness of the fault damage zone and core. The mesoscopic structural study was integrated with microstructural analyses, with description of the microstructures of the main components of the fault zone such as protolith, damage zone and fault core.

3.1. Architecture of the fault zone

The overall architecture of the fault (Figs. 3 and 4) is a protolith, an asymmetric damage zone and a fault core. In the studied segment of the structure, the fault core is clearly bounded by two non-parallel slip surfaces. The upper main slip surface (54/228) is striated, the orientation of slickensides on polished surface oriented 43/260, thus defining a normal-oblique slip fault. Conversely the lower main slip surface which is steeper with an

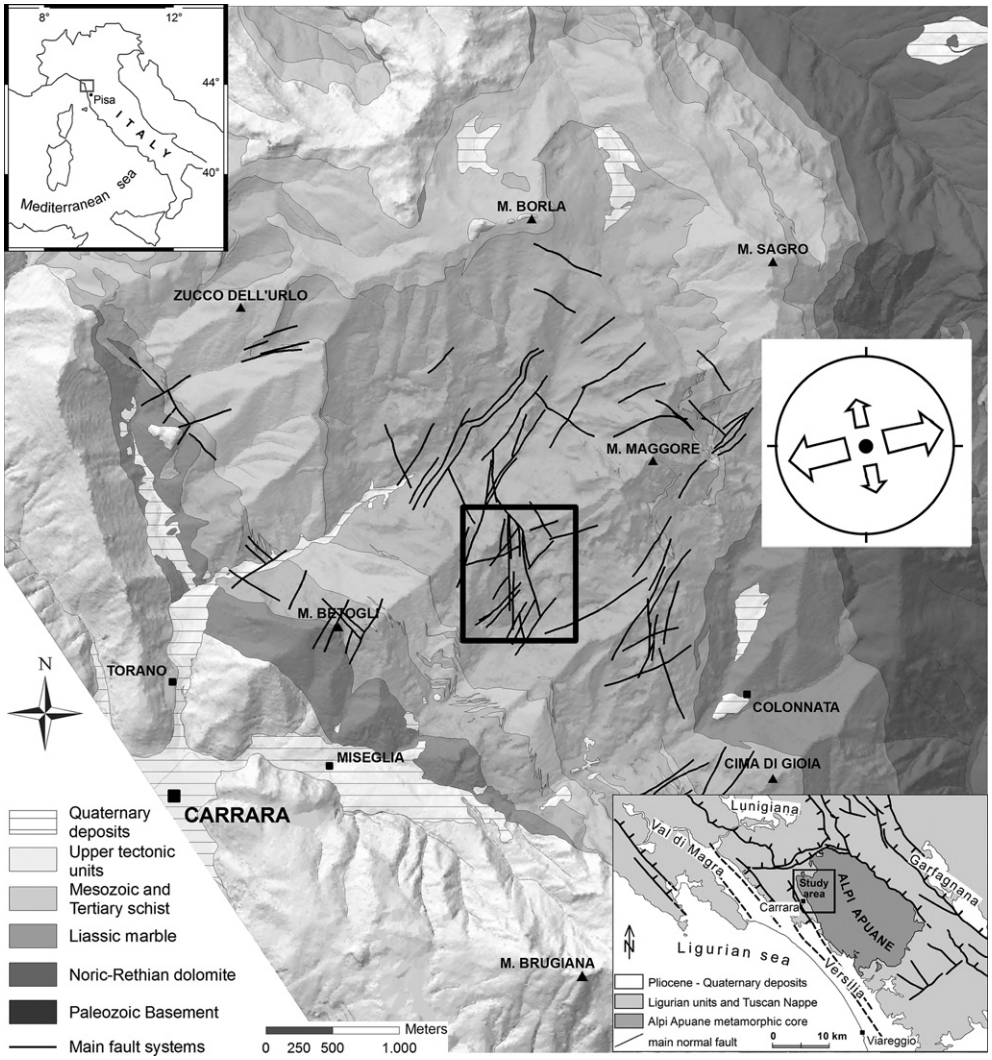

Fig. 1. Simplified geological map of the Carrara area showing the study area (black rectangle) in the Alpi Apuane. Principal directions of deformation for the normal faulting event are indicated by block arrows (Ottria and Molli, 2000).

attitude of 63/264. The absence of distinctive markers in the footwall- and hangingwall blocks precludes direct estimates of fault displacement. On the basis of the general relationships between maximum displacement/fault length and thickness/displacement (e.g. Watterson, 1986; Blenkinshop and Rutter, 1986; Hull, 1988; Blenkinshop, 1989; Evans, 1990; Kim and Sanderson, 2005), the studied structure and related system could have a maximum displacement of few decameters and a downward extension of at most few hundred meters. This agrees with regional data, which show at the scale of the Carrara marble basin (and more general in the whole Alpi Apuane) displacements along normal faults up to tens of meters.

3.2. Protolith

Outside the fault zone, the protolith is a white marble (commercial marble varieties "ordinary marble" Meccheri et al., 2007) in the footwall block, whereas in the hangingwall block, striped grey marble (commercial marble varieties "cloudy-like marble") is predominant.

The protolith marble (sample To-4, Fig. 5a) shows a very common microstructure observable in the Carrara marble basin (Molli and Heilbronner, 1999; Molli et al., 2000), consisting of an aggregate of equigranular polygonal grains (granoblastic or "foam" microstructure) with straight to slightly curved grain boundaries that meet at triple points with angles of nearly 120°. The average grain size is in the order of 250 μm. No crystallographic or shape preferred orientation can be easily observed under the microscope, and the density of the mechanical twinning (e-twins) is very low. No evident microfractures either of intragranular or intergranular types can be recognized.

3.3. Damage zone

In the 4 m immediately adjacent to the upper slip surface, fault-related structures in the hangingwall only comprise centimeter-wide and meter-long calcite–quartz veins, which are observed in two main orientations, respectively at high angle (c. 40°) and at low angle (c. 5–15°) to the main fault with an attitude sub-parallel to the fault trace (Fig. 3b). However, the presence only of artificial vertical or horizontal outcrops precludes the collection of a large amount of attitude data of these structures. In the hangingwall domain, at a pluridecameter-scale, a system of meter spaced joints, and minor faults, exhibits a mean density of 0.9 fractures for meter (Fig. 4).

The damage zone is well developed and observable only in the footwall block. It is formed by centimeter to decimeter-spaced

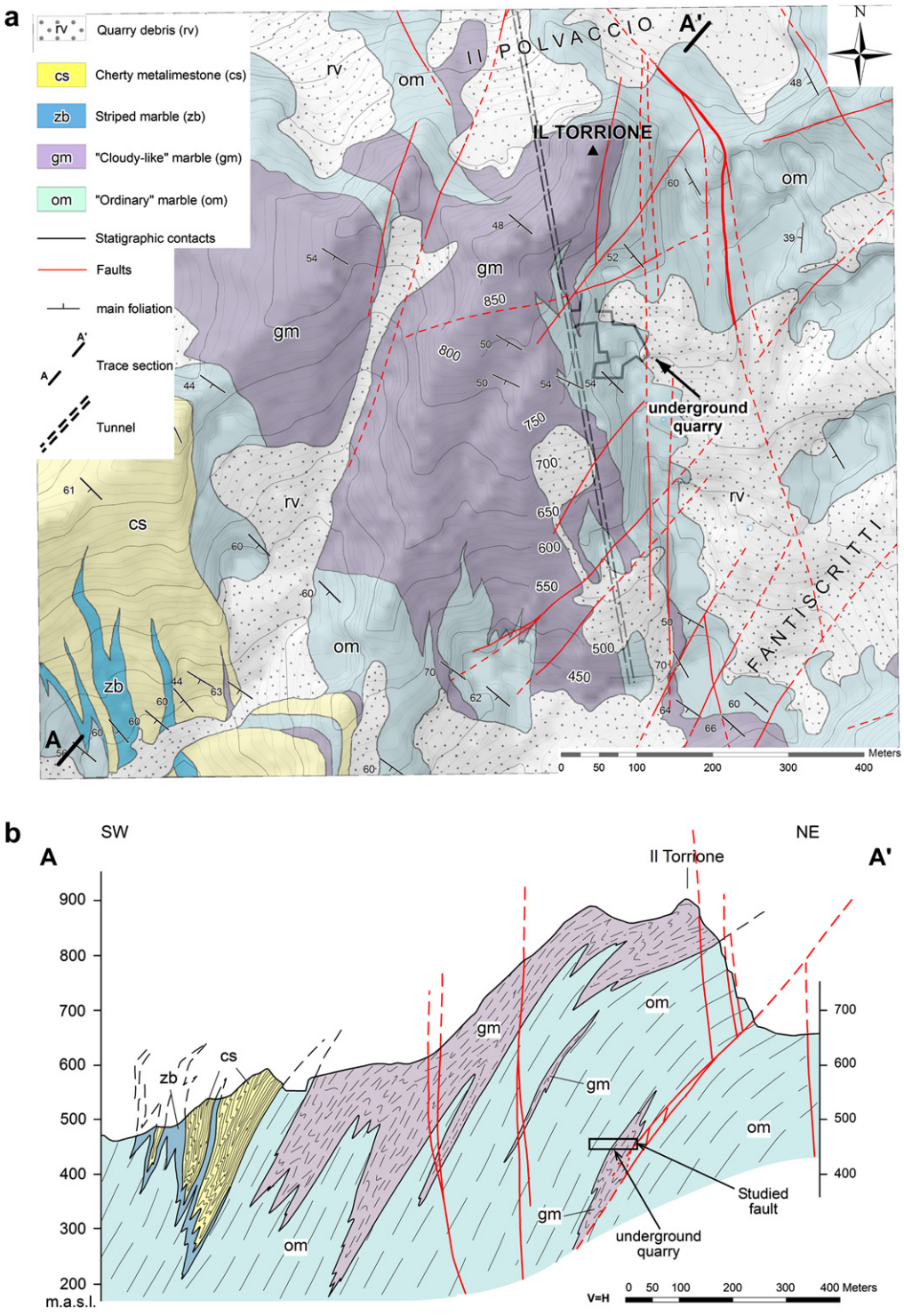

Fig. 2. (a) Geological map of the Fantiscritti basin and (b) geological cross section A–A′ with location of the normal fault studied.

anastomosing fractures, with a mean density of 21.6 fractures for meter, belonging to four principal sets (A, B, C and D). These sets compose a three-dimensional fracture pattern with two fracturing planes, respectively, parallel (A) and normal (C and D) to the strike of the master fault, and a subordinate set at 40° clockwise (B) to the fault. A system of millimeter to centimeter-wide calcite/quartz veins occurs in the footwall block sub-parallel, or at a high angle, to the master fault.

The observable trace of the upper slip surface is characterized by a centimeter-wide rim clearly recognizable by its anomalous lighter pinkish colour and appearance compared with the surrounding marble (Fig. 3c). Sample To-7 (Fig. 5b) is representative of this rim, and has been collected in the hangingwall at an approximately horizontal distance of 4 cm from the upper, fault core bounding, slip surface. Sample To-7 displays a microstructure different from those of the host marbles (e.g. sample To-4). It is characterized by

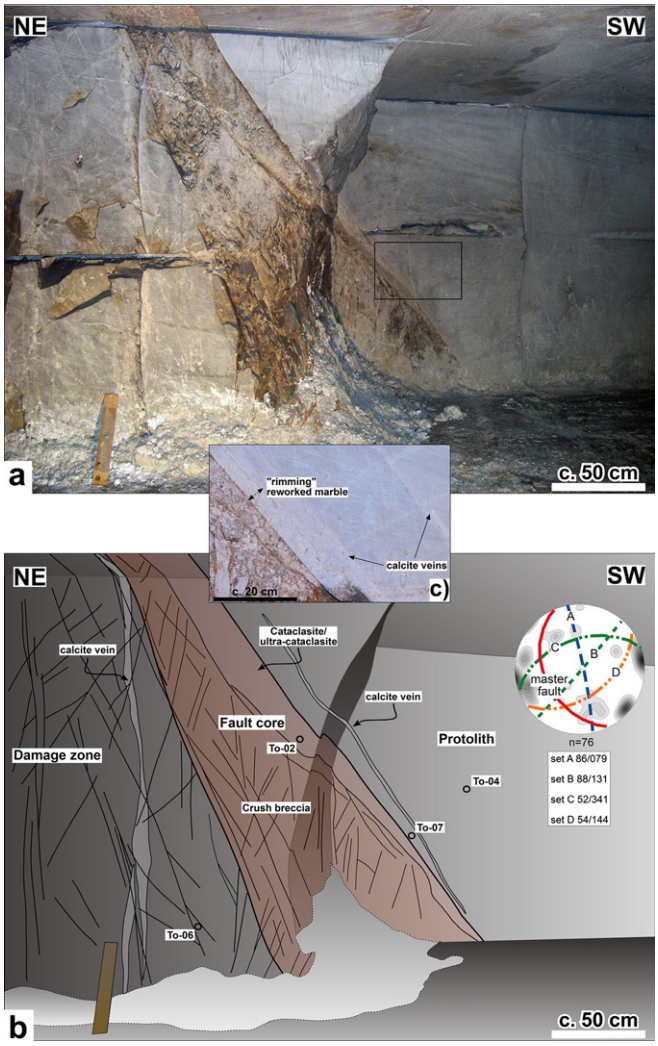

Fig. 3. Photo (a) and schematic sketch of the structural components of the fault studied (b). Equal area projection (Schmidt diagram, lower hemisphere) of the master fault with fractures set sinto the damage zone (a). Locations of the samples described in the text are indicated. In (c) the upper main slip surface is shown in detail, with calcite shear veins and "rimming" reworked marble in the hangingwall block (see text for details).

a high density of mechanical twin of rectilinear and lenticular-shapes, some of which taper within the crystals.

Sutured grain and twin boundaries, together with a second generation of fine grained calcite (size c. 10 μm) at the border of larger original coarse grains (size c. 250 μm), are evident (Fig. 5b).

Similar microstructures occur in marble from the footwall damage zone (Fig. 5c). Here a granoblastic polygonal microstructure with a high density of mechanical twins (sample To-6) is observed. Although less intense than in the hangingwall sample (To-7), evidence of reworking of the original foam microstructure is demonstrated by sutured grain boundaries (wave length c.10 μm). Intergranular and intragranular microfractures are widespread and represented by fine grained (less than 10 μm) crushed calcite (Fig. 5c).

3.4. Fault core

The approximately 1 m thick fault core, bounded both at the top and the bottom by principal slip surfaces, is characterized by fault rocks defined, after Sibson (1977), as crush breccia, protocataclasite and cataclasite/ultracataclasite on the basis of the size of fragments and percent of matrix. Cataclastic fault rocks show angular to sub-angular clasts (from centimeter to millimeter in size) embedded within a fine grained orange–brownish matrix.

The cataclasite (sample To-2) comprises fragments of marble with variable size from centimeter down to 100–200 μm surrounded by a finer grained matrix (Fig. 5d,e). The matrix is composed of calcite observable both as sub-crystal sized crushed calcite grains from the host rock and as newly formed/crystallized calcite. The matrix appears to be enriched in oxides and clay minerals (Fig. 5d–f). Polycrystalline calcite clasts (host marble-derived) show evidence of twinning, kinking and twin boundary migration, similar to the microstructures found within the tapering marble present in both hangingwall and in the footwall damage zone (Fig. 5e). Coarse (mm in size) calcite fragments, possibly vein-derived, can be also observed together with millimeter-thick calcite/quartz later veins which locally overprint clasts and matrix, often associated with stylolite seams developed at the clasts/matrix interfaces (Fig. 5f).

4. Chemical and isotopic data

4.1. Samples

In order to constrain the role and types of fluids possibly involved during deformation, geochemical and isotopic analyses were performed on fault zone samples collected along a profile that goes from protolith to cataclastic fault core (Figs. 6–8). Samples include: (i) the undeformed marble protolith (To-4), collected at about 55 cm from the main upper slip surface; (ii) fractured marble (To2D), at the base of the inner fault core and toward the boundary of the damage zone, and from the crushed breccia at about 30 cm from the upper slip surface; (iii) three specimens of the fault core with different matrix/clast proportions. To2A is from ultra-cataclasite whereas To2B and To2C are from the cataclasite near the main upper slip surface. Clasts and matrix were hand-picked under a binocular microscope, and then analyzed. It must be noted that despite the care taken, all matrix separated in such a way contain some minute marble clasts. Samples of calcite/quartz veins, collected from different structural components of the fault zone (hangingwall and footwall damage zone), were also analyzed.

4.2. Chemical and isotopic analytical methods

Analyses of major and trace elements were carried out by XRF spectrometry. With regards to carbon and oxygen isotope composition analyses, carbon dioxide was quantitatively extracted from calcite by treatment with 100% H_3PO_4 at 25 °C following the method of McCrea (1950), and then analyzed by mass spectrometry. The isotopic compositions are reported in the δ-notation, per mil (‰), relative to V-PDB for carbon and V-SMOW for oxygen respectively. The precision of these measurements is within ± 0.1‰. $^{87}Sr/^{86}Sr$ ratios of the calcite fraction from the samples were determined after leaching with 40% acetic acid at room temperature. Sr was extracted from the leachate on a cation exchange resin, then converted after elution to $Sr(NO_3)_2$ for thermal ionization mass spectrometric analysis. The precision of Sr isotope ratio analyses was within ±0.00002. The measured ratios were normalized to a $^{87}Sr/^{86}Sr$ ratio of 0.1194 for natural strontium, and to a $^{87}Sr/^{86}Sr$ ratio of 0.710200 (±0.000012) for NBS 987 $SrCO_3$ standard. The results of the chemical and isotopic analyses are reported in Tables 1 and 2. Data recovered from samples pertaining to different structural components of the fault zone will be discussed separately.

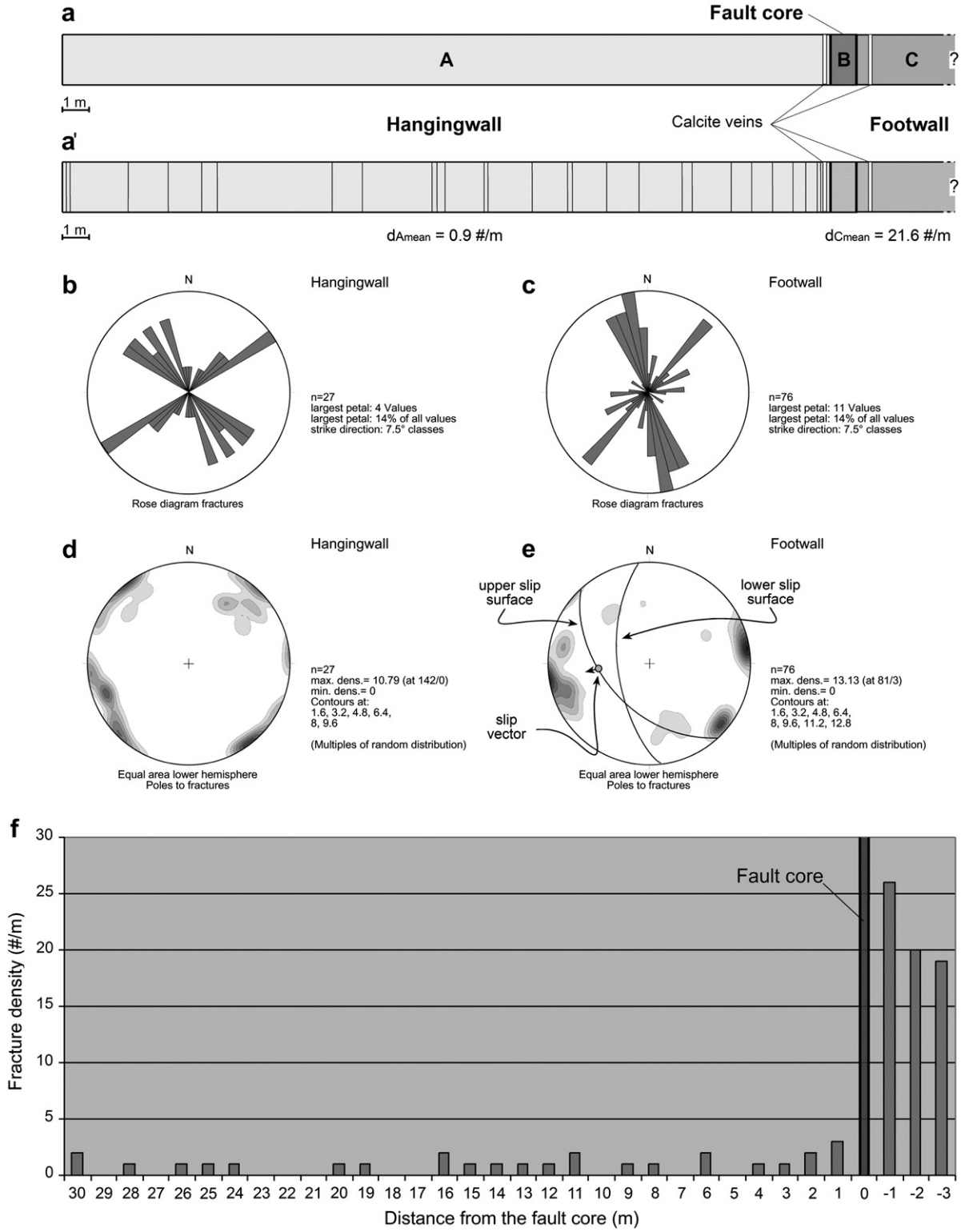

Fig. 4. (a) Scan line across the investigated fault zone. Structural location concerning principal fault zone components: A-hangingwall, B-fault core, C-footwall damage zone; (a') position of the fractures and minor faults within the fault zone; (b, c) Rose diagrams showing trend of the fractures in the hangingwall (b) and footwall damage zone; (d, e) Equal area plots (Schmidt diagram, lower hemisphere) for fractures in hangingwall (d) and footwall (e) damage zone, in (e) trace of upper and lower slip surfaces bounding the fault core are indicated as well as the mean slip vector; (f) Distribution and frequency of the fractures (per meter) vs. distance from the fault core.

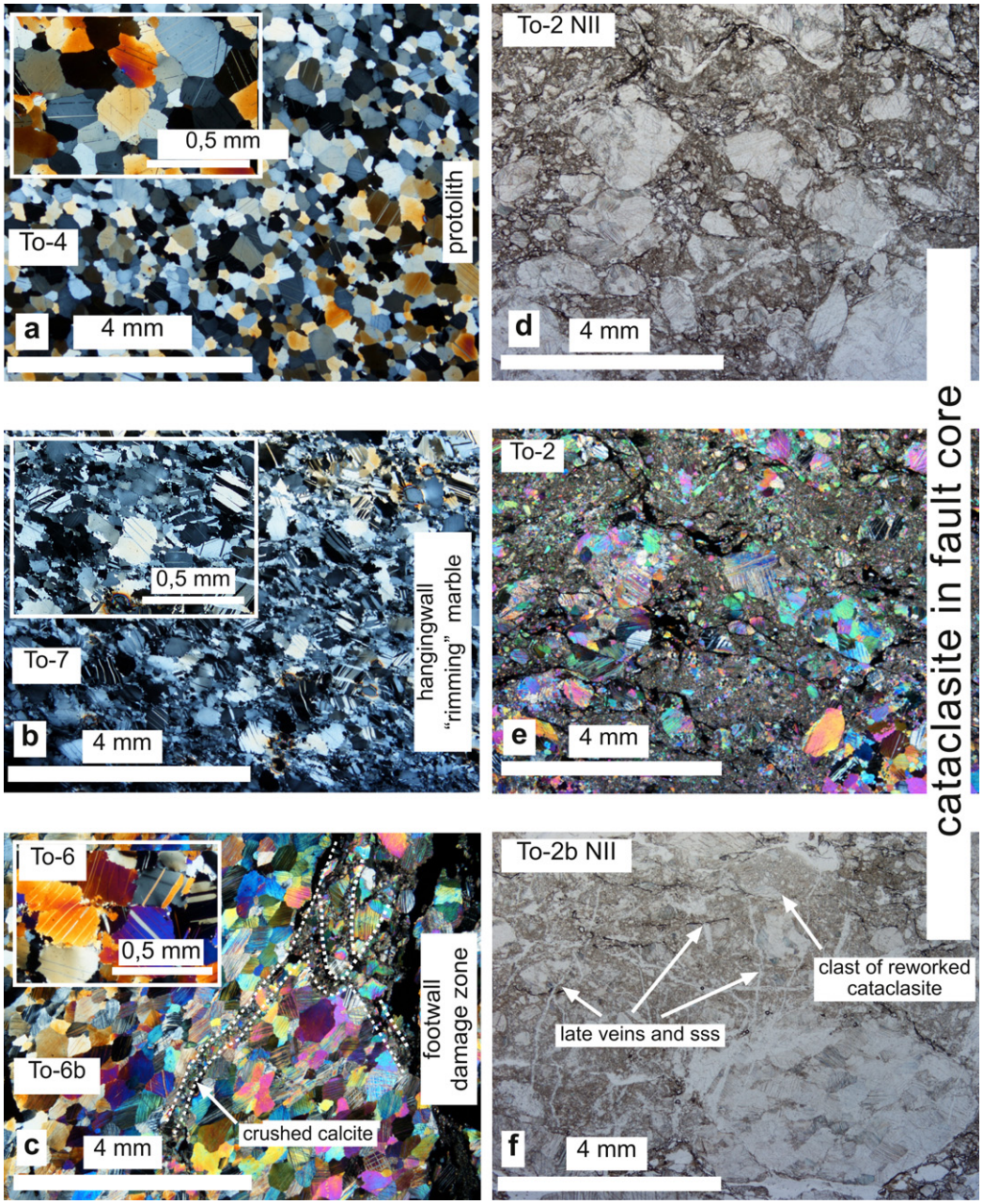

Fig. 5. Microstructures associated with different fault zone components (pictures are ultrathin sections, <5–10 μm, and cross-polarized if not indicated otherwise). (a) Granoblastic or "foam" microstructure typical of statically recrystallized Carrara marble observable in the protolith (sample To-4) (Molli and Heilbronner, 1999; Molli et al., 2000); (b) sample of hangingwall "rimming" domain (sample To-7) (4 cm from the upper slip surface), showing evidence of dynamic recrystallization, high density of mechanical twinning, sutured grain boundaries and twin boundary migration; (c) sample of damage zone domain (To-6), microstructure similar to those of To-7 although with less microfabric reworking. Microcracking and sub-millimeter cataclastic crushed calcite domains can be observe; (d, e, f) micrographs of cataclasite showing angular to subrounded marble and vein-derived clasts. Clasts of marble and calcite veins internally show abundant evidence of crystal-plasticity (micrograph (e) in natural light), (f) arrowed: clast of reworked cataclasite, and different generation of calcite veins (within clasts) and cutting it. All these features testify multiple cycles of activity of the fault core ending with a late stage of veining associated with stylolite solution seams (sss).

4.3. Marble from protolith and crush breccia

Massive protolith marble (sample To-4) is made up of nearly pure calcite, with an Sr content of 192 ± 7 ppm. No Mn was detected. Pb, Zn and Cu average 7 ppm, 21 ppm and 32 ppm, respectively. These chemical data are similar to those observed in massive marble specimens associated to other cataclastic structures in the Alpi Apuane area (Cortecci et al., 2003). In all these specimens, however, the Zn concentration is definitely higher than that measured in marble far from any significant brittle structure (5.6–8.8 ppm Zn; Herz and Dean, 1986). The $\delta^{13}C$ of +2.2‰ and $\delta^{18}O$ of +28.7‰ values and the $^{87}Sr/^{86}Sr$ ratio of 0.70790 (sample To4-1) nicely fit with available data on massive Liassic marble of Alpi Apuane ($\delta^{13}C = +2.18 \pm 0.25$‰; $\delta^{18}O = +28.8 \pm 0.48$‰; $^{87}Sr/^{86}Sr = 0.70790 \pm 0.00011$; Herz and Dean, 1986).

The sample from crushed breccia (To2D) is similar to protolith marble, even if lower in Sr by 18%, and by 0.6–1.5‰ in $\delta^{13}C$ and $\delta^{18}O$. Its $^{87}Sr/^{86}Sr$ ratio of 0.70791 matches the mean of "normal" Carrara marbles.

4.4. Fault core

Data from the analyzed samples of the fault core will be presented beginning from those concerning the crush breccia and

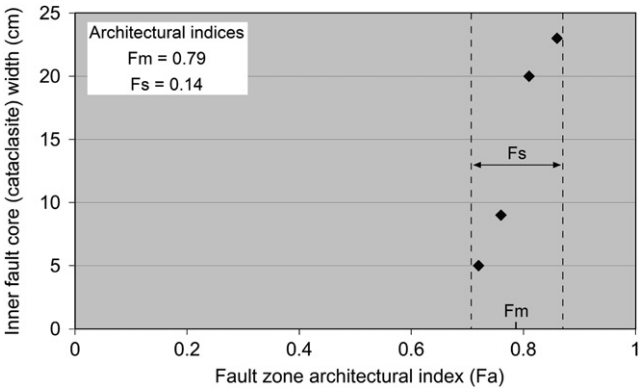

Fig. 6. Geometric parameters and architectural index of permeability modified from Caine et al. (1996). In our studied fault, since footwall damage zone cannot be completely observed and the distribution of fractures is clearly asymmetric, we use the index Fa (observable damage zone width/inner cataclastic fault core + outer crushed fault core + ob.damage zone width) vs. inner fault core width. According to this, the fault zone has a permeability index of a combined conduit/barrier.

finishing with those from the ultracataclasite present near the main slip surface.

To2C – Coarse and fine clasts within this sample show quite similar content of major elements. The same applies to the trace elements, excluding Cu and Pb which appear to be appreciably enriched in fine clasts. All clasts have, on average, lower $\delta^{13}C$ (+0.8‰) and $\delta^{18}O$ (+26.8‰) values than sample To2D from the crushed zone (+1.1‰ for carbon and +27.5‰ for oxygen), with the lowest values found in fine clasts. The matrix separates show lower $\delta^{13}C$ (+0.39 and +0.53‰) and $\delta^{18}O$ (+23.8 and +26.3‰). Clasts and matrix show nearly equal $^{87}Sr/^{86}Sr$ ratios of 0.70822–0.70829, which are significantly higher than in normal marble and in sample To2D.

To2B – Clast and matrix separates have consistent chemical and isotopic values. Compared to the clasts, matrix samples are enriched in Mn (126–180 ppm), Fe_2O_3 (0.59–0.63%), Al_2O_3 (0.97–1.9%) and SiO_2 (3.5–6.0%). The $\delta^{13}C$ and $\delta^{18}O$ values of clasts are respectively between –0.8 and +0.5‰, and +25.0 and +26.0‰, with the lowest values found in the fine clasts. Clasts and matrix show slightly lower $\delta^{13}C$ and $\delta^{18}O$ values than those in sample To2C. On the other hand, the $^{87}Sr/^{86}Sr$ ratios vary between 0.70826 and 0.70829, with no differences between clasts and matrix. They are also nearly equal to those of sample To2C.

To2A – Clast and matrix separates show a comparable chemistry with the host marble. The matrix, however, has high Mn (232 ppm), Fe_2O_3 (0.74%), Al_2O_3 (2.4%) and SiO_2 (9.6%), comparable with that from sample To2B. Clasts and matrix show comparable $\delta^{13}C$ (−0.3 to +0.6‰) and $\delta^{18}O$ (+24.9 to +26.8‰) values, which in turn are nearly equal to those in sample To2B. The $^{87}Sr/^{86}Sr$ ratios vary within the 0.70820–0.70830 range, as found also in sample To2A.

4.5. Veins

Veins in the different structural components of the fault zone mostly consist of calcite (with minor quartz), excepting for the sample To-21 (Table 2) which is obtained from a vein parallel to the fault. Samples To-8, To-9 and To-11 are all from the same vein, which is cut by the fault, whereas sample To-16 is from a vein just at the border with the host marble. Mesoscopic appearance is micro- (To-8, To-9A, To-16) to macrocrystalline (To-9, To-11) and translucent (To-21). All but one sample show a similar chemical composition, with small differences due to Si–Al–Fe-mineral impurities. The latter are higher in sample To-21, which also is the richest one in Sr. All samples are chemically indistinguishable from massive marble (Fig. 8b, and Herz and Dean, 1986). Their isotopic composition ($\delta^{13}C = +1.95 \pm 0.2$‰; $\delta^{18}O = +28.9 \pm 0.3$‰) is also nearly identical to that of massive marble ($\delta^{13}C = +2.2$‰; $\delta^{18}O = +28.8$‰; Fig. 8b, and Herz and Dean, 1986), but quite different from that of calcite, collected from the cataclasite core.

5. Discussion and interpretation of chemical and isotopic data

5.1. $\delta^{13}C$ vs. $\delta^{18}O$ relationships and $^{87}Sr/^{86}Sr$ ratios

The nearly progressive decrease both $\delta^{13}C$ and $\delta^{18}O$ found in samples collected from marble protolith to damage zone to cataclasite (clasts and matrix) of the fault core (Fig. 7b,c) suggests that fluids depleted in ^{13}C and ^{18}O and fluid–rock exchange processes were involved during localization of deformation. The lowest $\delta^{18}O$ signature shown by the microcrystalline calcite in the cataclasite matrix supports its precipitation from these fluids. On the whole, marble (protolith and fractured marble in the crush breccia) and clast samples of the fault core display a rather good linear $\delta^{13}C$ vs. $\delta^{18}O$ correlation. Both carbon and oxygen isotope values span between −0.8 and +2.2‰ and between +24.9 and +27.7‰, respectively (Fig. 8b). With respect to the protolith marble, clasts are variously depleted in heavy isotopes, as expected from interaction with external fluids or other processes such as mixing with secondary calcite or thermal decomposition. Matrix samples do not show any clear $\delta^{13}C$ and $\delta^{18}O$ correlation. The isotopic (and chemical) similarity with protolith marble of the vein calcites in the damage zone may be explained by a model in which: (1) the precipitating fluid interacted with the marble modifying its original chemical and isotopic composition, (2) most calcium and carbonate in the fluid were provided by marble, and (3) different fluids were involved in the vein calcite precipitation ($\delta^{13}C = +1.7$ to 2.1‰; $\delta^{18}O = +28.7$ to +29.3‰) and in the fault core matrix formation ($\delta^{13}C = -0.22$ to +0.53‰; $\delta^{18}O = +23.76$ to +26.27‰).

The $^{87}Sr/^{86}Sr$ (Fig. 7d) ratios are nearly identical in clasts and matrix, where they are considerably enriched in radiogenic strontium with respect to marble from the protolith and crush breccia. This suggests that the intervening fluids interacted with siliciclastic rocks during circulation. In the Alpi Apuane, these rocks constitute the Paleozoic basement, and other occurrences of Lower Triassic age, overlaying the basement itself. In addition, some matrix samples display a much higher concentration of Fe and Mn than in clasts, as well as in the protolith marble, due to their direct precipitation from the fluids. These data point to a provenance of the fluids from deeper formations that may include the basement (up to 0.27% MnO and up to 8.5% Fe_2O_3, excluding a black phyllite with 83% Fe_2O_3; Cortecci et al., 2003). Additional provenance may include overlying carbonate formations of the Grezzoni (dolomite ± calcite; mean 106 ppm Mn and 0.47% Fe_2O_3; $^{87}Sr/^{86}Sr = 0.707651 \div 0.709007$; $\delta^{13}C = +2.2 \pm 0.9$‰) and Marmi Dolomitici (calcite ± dolomite; mean 49 ppm Mn and 0.23% Fe_2O_3; $^{87}Sr/^{86}Sr = 0.707651 \div 0.708404$; $\delta^{13}C = +1.5 \pm 0.7$‰) (Cortecci et al., 1999).

5.2. Mn vs. Fe relationships

The plot of Fig. 8a shows a positive trend between Mn and Fe in clasts and matrix, with the highest concentrations in the latter elements. Due to the occurrence of a variable fraction of clasts in the matrix, the data distribute along a "mixing" line between

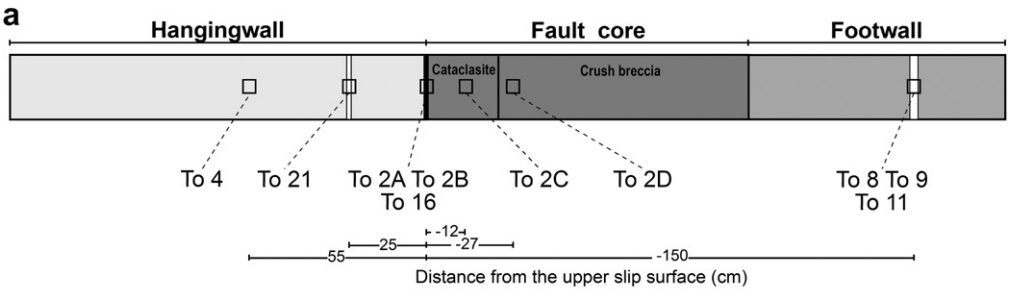

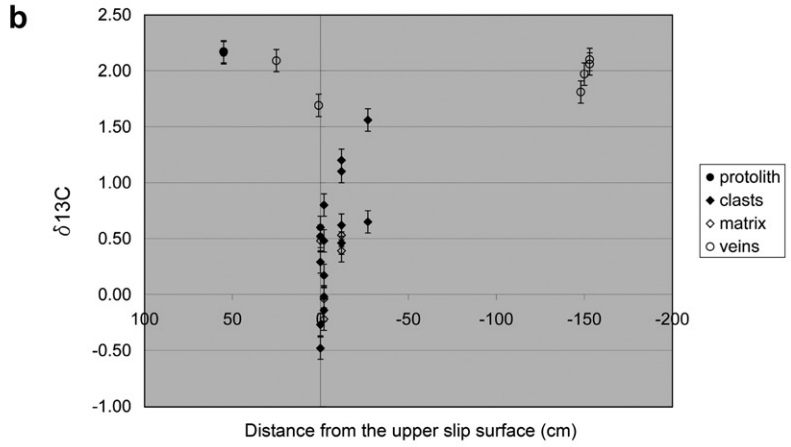

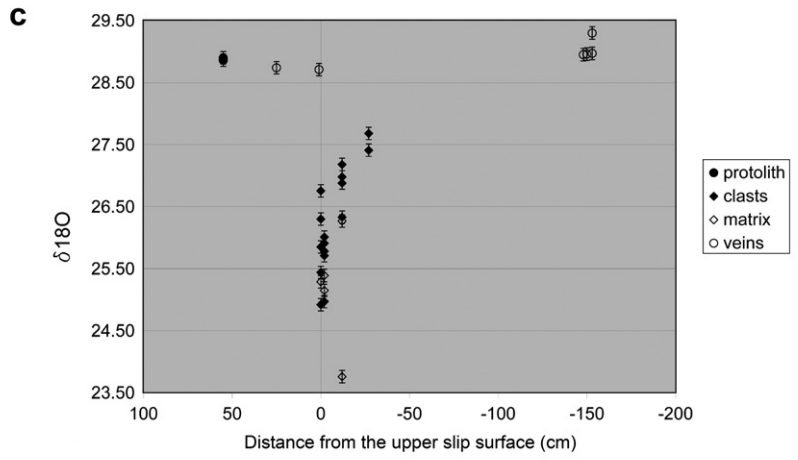

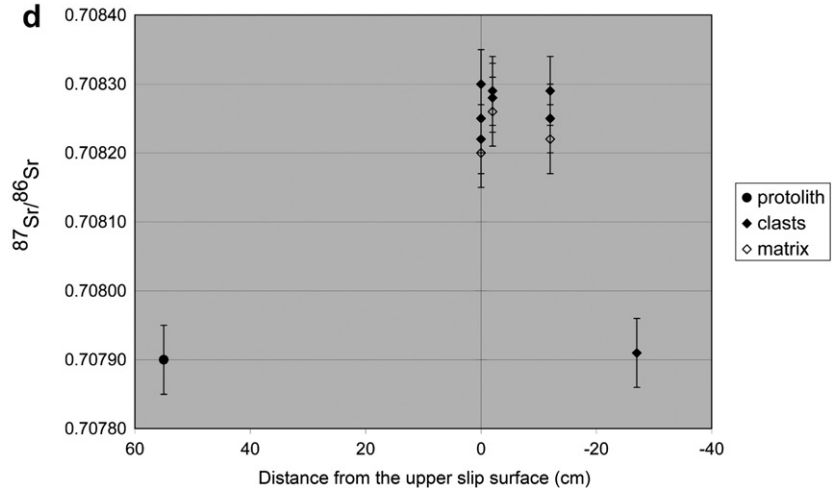

Fig. 7. (a) Locations for geochemically investigated samples from hangingwall protolith and fault core comprising veins. (b, c, d) $\delta^{13}C$, $\delta^{18}O$ and $^{87}Sr/^{86}Sr$ vs. distance from the upper main slip surface.

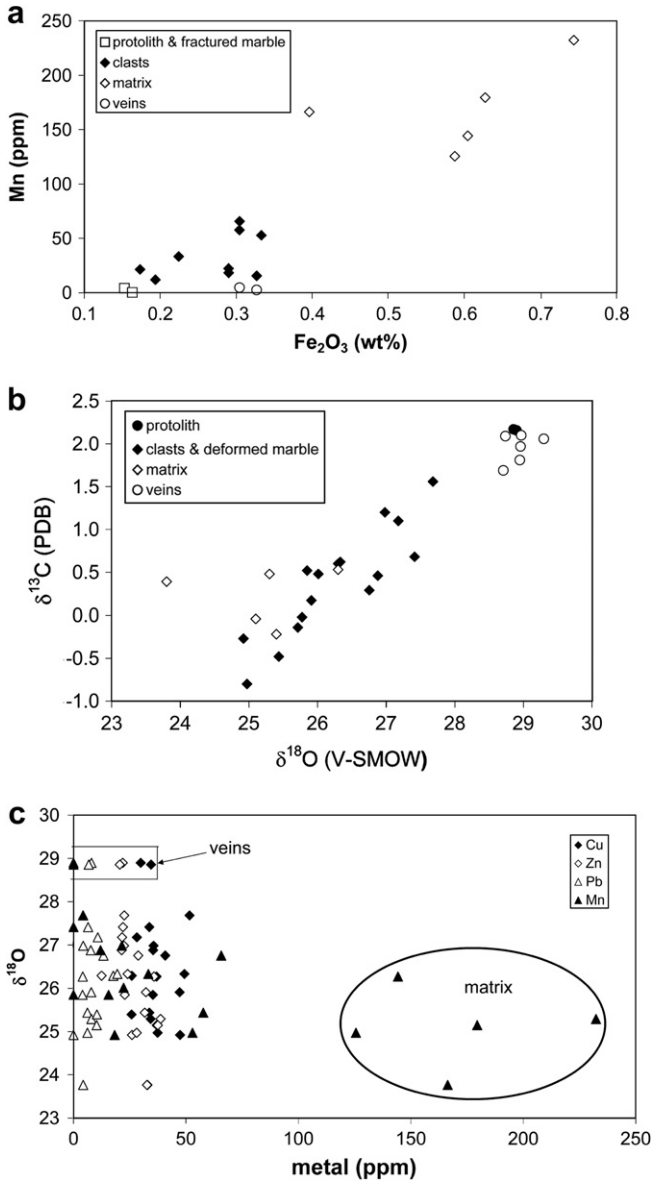

Fig. 8. (a) Scatter plot for Mn and Fe concentrations in the protolith and damage zone (massive and fractured marble) cataclasites (clasts and matrices) and veins; (b) scatter plot between $\delta^{13}C$ and $\delta^{18}O$ values in the analyzed samples; (c) $\delta^{18}O$ signature vs. metal content (Cu, Zn, Pb, Mn).

a component low in Mn and Fe (marble-derived clasts) and a component high in Mn and Fe, i.e. syntectonic calcite with 232 ppm Mn and 0.74% Fe_2O_3 (see Table 2). Matrix is also enriched in Al and Si, supporting the occurrence of Al-silicates along with Mn–Fe impurities.

5.3. $\delta^{18}O$ vs. metal relationships

Mn, Cu, Zn and Pb do not show any relation with the $\delta^{18}O$ values of protolith and damage zone marble, fault core clast and matrix samples. However, all Mn concentrations higher than about 120 ppm are found in matrix samples (Fig. 8c). The total base metal concentration values do not show any correlation with the isotopic parameters, as well. However the matrix samples have on average higher values compared to the other samples.

5.4. Mathematical modeling of carbon and oxygen isotopic data

The good linear $\delta^{13}C$ and $\delta^{18}O$ correlation ($R^2 = 0.89$) between protolith marble, crush breccia and clasts (Fig. 8b) may be simply explained by the mixing between pieces of protolith marble and secondary microcrystalline calcite matrix depleted in both ^{13}C and ^{18}O. However, this interpretation implies that the calcite matrix from the cataclasite should have $\delta^{13}C$ considerably lower than $-1‰$. This apparently contrasts with the observed $\delta^{13}C$ signature of matrix calcite samples from the studied cataclasite with values between -0.22 and $+0.53‰$ (mean $+0.23‰$; $n = 5$), as well as from other previously investigated cataclasites in the Alpi Apuane with $\delta^{13}C$ values of -0.6 to $+1.1‰$ (mean $+0.37$; $n = 7$; Cortecci et al., 2003). Therefore, alternatives need to be explored. According to the experiments on Carrara marble carried out by Han et al. (2007), decomposition of calcite under dry conditions due to frictional heating may be a common phenomenon in natural carbonate faulting at temperatures as high as 900 °C, or more. Thermal calcite decomposition due to frictional heating could produce heavy effects on fault dynamic weakening (Han et al., 2007). Moreover, it leads to the production of CO_2 enriched in heavy ^{13}C and ^{18}O, thus lowering the starting isotopic composition of marble clasts (e.g. Shieh and Taylor, 1969). Since our clasts are the products of faulting and breaking occurred, likely, in a dry environment, they should have experienced a high temperature frictional regime, with a corresponding partial decomposition and the related isotopic effects. In fact, all data fit the isotopic effects derived from the decomposition model at temperatures from 500 to 750 °C (Fig. 9a). Both closed system and open system decarbonation models were applied to protolith marble ($\delta^{13}C = +2.2‰$, $\delta^{18}O = +28.9‰$), then the isotopic effects on remaining calcite were computed during progressive decomposition using the governing equations given by Taylor (1986) for metamorphic volatilization processes. In the modeling, CO_2 was assumed to be in equilibrium with calcite, and the isotope fractionations of Chacko et al. (1991) were applied. The governing equations for both carbon and oxygen isotopes are:

$$\delta_f = \delta_i + (F - 1)\,1000 \ln \alpha (\text{closedsystem})$$

$$\delta_f = \delta_i + 1000\,(F^{\alpha - 1} - 1)(\text{opensystem})$$

where α is the carbon or oxygen isotope fractionation factor (dependent on temperature) between CO_2 and $CaCO_3$, and F is the fraction of remaining clast.

However, the dry thermal decomposition cannot influence the original $^{87}Sr/^{86}Sr$ ratio of marble. Unfortunately this is not the case of the clasts studied, which are appreciably enriched in radiogenic Sr. Therefore, even if thermal decomposition might have possibly played a minor role during the first phase of faulting, deformation in presence of fluids should be admitted. This scenario also better fit the meso- and microstructural features of our samples. It is then suggested that fluids should be invoked to explain the carbon, oxygen and strontium isotopic composition of the clasts. The carbon and oxygen isotopic effects expected from the inferred fluid–clast interactions are modeled in Fig. 9a for exchange in both closed and open systems. We applied the mass balance equations (integrated form) reported in Zheng and Hoefs (1993), with an initial meteoric fluid $\delta^{18}O$ value of $-7‰$ for the area of interest (Mussi et al., 1998) and an initial $\delta^{13}C$ value of $-12‰$ for bicarbonate in the fluid (a likely value in a terrestrial carbonate setting; Vogel and Ehhalt, 1963). Under these conditions, the model fits the data distribution if the simulation is performed at 70 °C in fluids with a bicarbonate mole fraction (X_{HCO_3}) in the range of 0.5–0.8. The isotope fractionations at 70 °C are from Ohomoto and Rye (1979) for carbon and O'Neil et al. (1969) for oxygen.

Table 1
Chemical and isotopic compositions of the fault zone components from protolith to fault core.

Sample	Notes	SiO_2	TiO_2	Al_2O_3	Fe_2O_3	MgO	CaO	Na_2O	K_2O	P_2O_5	LOI	Cu	Zn	Rb	Sr	Pb	Mn	$\delta^{13}C$	$\delta^{18}O$	$^{87}Sr/^{86}Sr$
		wt%	wt%	wt%	wt%	wt%	wt%	wt%	wt%	wt%	wt%	ppm	ppm	ppm	ppm	ppm	ppm	‰	‰	
To2A-1	CC	n.d.	0.11	0.60	0.18	0.64	55.01	0.07	0.00	0.01	43.88	35	23	10	141	4	n.d.	0.52	25.85	n.a.
To2A-1bis	CC	0.28	0.13	0.57	0.33	0.52	54.72	n.d	0.02	0.01	43.30	26	13	10	167	18	16	0.60	26.30	0.70822
To2A-2	FC	0.28	0.12	0.85	0.30	0.60	54.70	0.08	0.08	n.d.	42.89	41	29	14	147	13	66	0.29	26.76	n.a.
To2A-3	FC	0.31	0.11	0.83	0.30	0.58	54.42	0.07	0.08	0.01	43.17	34	32	15	114	6	58	−0.48	25.44	0.70825
To2A-4	FC	n.d	0.11	0.70	0.29	0.63	56.04	0.07	n.d.	0.02	42.04	47	26	7	133	n.d.	18	−0.27	24.92	0.70830
To2A-M	M	9.64	0.16	2.42	0.74	0.97	45.19	0.08	0.58	0.03	40.09	34	39	25	153	8	232	0.48	25.29	0.70820
To2B-1	FC-CC	n.a.	n.a.	n.a.	n.a.	n.a.	n.a.	n.a.	n.a.	n.a.	n.a.	n.a.	n.a.	n.a.	n.a.	n.a.	n.a.	0.48	26.01	0.70829
To2B-1bis	FC-CC	n.d.	0.11	0.70	0.29	0.63	56.01	0.09	0.01	0.02	42.04	47	32	15	159	8	22	0.17	25.91	n.a.
To2B-2	FC	0.56	0.12	0.87	0.33	0.66	54.17	0.05	0.09	0.01	42.99	37	28	13	151	6	53	0.80	24.97	0.70829
To2B-3	FC	n.a.	n.a.	n.a.	n.a.	n.a.	n.a.	n.a.	n.a.	n.a.	n.a.	n.a.	n.a.	n.a.	n.a.	n.a.	n.a.	−0.02	25.78	0.70828
To2B-4	FC	n.a.	n.a.	n.a.	n.a.	n.a.	n.a.	n.a.	n.a.	n.a.	n.a.	n.a.	n.a.	n.a.	n.a.	n.a.	n.a.	−0.14	25.71	n.a.
To2B-2Mbis	M	3.47	0.16	0.97	0.59	0.54	50.60	0.05	0.31	0.01	43.17	26	25	17	116	10	126	−0.22	25.39	0.70826
To2B-M	M	6.00	0.14	1.90	0.63	0.88	48.75	0.06	0.47	0.02	41.04	37	38	20	136	10	180	−0.04	25.15	0.70828
To2C-1	CC	n.d.	0.10	0.54	0.16	0.73	54.77	0.07	0.00	n.d.	43.51	28	22	10	157	11	n.d.	1.10	27.18	n.a.
To2C-2	FC	n.d.	0.10	0.67	0.22	0.69	54.93	0.07	0.02	0.01	43.16	49	24	11	160	20	33	0.62	26.33	n.a.
To2C-3	FC	n.d.	0.10	0.58	0.19	0.67	54.87	0.07	n.d.	0.01	43.40	35	21	18	162	8	12	0.46	26.88	0.70829
To2C-4	FC-CC	n.d.	0.09	0.56	0.17	0.66	55.08	0.05	n.d.	0.00	43.28	36	23	11	207	4	22	1.20	26.98	0.70825
To2C-5M	M	1.58	0.12	1.14	0.40	0.69	52.67	0.05	0.20	0.03	43.01	33	33	25	178	4	166	0.39	23.76	0.70825
To2C-M	M	7.14	0.14	1.93	0.60	0.93	47.97	0.07	0.43	0.02	40.67	37	36	21	170	4	144	0.53	26.27	0.70822
To2D-1	FM	n.d.	0.11	0.56	0.15	0.86	54.69	0.08	n.d.	0.10	43.43	52	23	14	171	4	4	1.56	27.68	n.a.
To2D-2	FM	n.d.	0.10	0.55	0.16	0.75	54.96	0.06	0.00	0.02	43.29	34	22	14	142	7	n.d.	0.65	27.41	0.70791
To4-1	U	n.d.	0.10	0.66	0.16	1.04	54.58	n.d.	0.03	0.01	43.31	30	22	14	186	8	n.d.	2.16	28.90	0.70790
To4-2	U	n.d.	0.10	0.57	0.16	0.98	54.58	0.06	n.d.	0.10	43.44	35	21	13	199	7	n.d.	2.17	28.86	n.a.

Protolith = U; Fault core: FM = fractured marble, CC = coarse clasts (c. 1 cm), FC = fine clasts (c. 1–2 mm), M = matrix. n.d. = not detected, n.a. = not analyzed.

Equations used for calculating the isotopic composition of altered calcite are, in an open system:

$$\delta^{13}C_{cal} = \left(\delta^{13}C^{i}_{HCO_3} + \Delta^{13}C^{cal}_{HCO_3}\right) - \left(\delta^{13}C^{i}_{HCO_3} + \Delta^{13}C^{cal}_{HCO_3} - \delta^{13}C^{i}_{cal}\right)e^{-(W/R)X_{HCO_3}}$$

$$\delta^{18}O_{cal} = \left(\delta^{18}O^{i}_{H_2O} + \Delta^{18}C^{cal}_{H_2O}\right) - \left(\delta^{18}O^{i}_{H_2O} + \Delta^{18}O^{cal}_{H_2O} - \delta^{18}O^{i}_{cal}\right)e^{-(W/R)}$$

and in a closed system:

$$\delta^{13}C_{cal} = \left[\delta^{13}C^{i}_{cal} + W/RX_{HCO_3}\left(\delta^{13}C^{i}_{HCO_3} + \Delta^{13}C^{cal}_{HCO_3}\right)\right] \Big/ \left[1 + (W/R)X_{HCO_3}\right]$$

$$\delta^{18}O_{cal} = \left[\delta^{18}O^{i}_{cal} + W/R\left(\delta^{18}O^{i}_{H_2O} + \Delta^{13}O^{cal}_{H_2O}\right)\right] \Big/ [1 + (W/R)]$$

where cal = calcite, i = initial composition, Δ = isotope fractionation factor (dependent on temperature) between calcite–bicarbonate (carbon isotopes) or calcite–water (oxygen isotopes), W/R = water to rock ratio in terms of atom percentage of carbon or oxygen in fluid (W) and rock (R), and X_{HCO_3} = mole fraction of bicarbonate in the fluid.

One may argue that at 70 °C the rate of oxygen isotopic exchange is slow, and then water and rock will maintain their original isotopic composition. This may be true at temperature lower than about 60 °C, but when the water is heated up to 80 °C, or more, a change in the oxygen isotope composition occurs due to the increasing rate of isotopic exchange (Gat, 1981). On the other hand, the data points do not fit the interaction model when higher temperatures and corresponding isotopic fractionations are introduced in the model.

During the fluid/marble interaction phase, cation exchange may take place providing calcium to the solution and promoting its saturation with respect to calcite. Therefore, the isotopic composition of carbon and oxygen in the calcite precipitated from the fluid is determined by the differences of its isotopic compositions with respect to that of the marble. Based on a mass balance approach, the $\delta^{13}C$ and $\delta^{18}O$ of calcite can be calculated as described in Zheng and Hoefs (1993) in terms of the initial isotopic signatures of the fluid, the isotopic fractionations between calcite and fluid at the chosen temperature, the water/rock ratio (W/R), and the differences between the initial and final δ-values ($\Delta^{13}C$ and $\Delta^{18}O$ differences) of the marble. Equations

Table 2
Chemical and isotopic compositions of the calcite veins.

Sample	Notes	SiO_2	TiO_2	Al_2O_3	Fe_2O_3	MgO	CaO	Na_2O	K_2O	P_2O_5	LOI	Cu	Zn	Rb	Sr	Pb	Mn	$\delta^{13}C$	$\delta^{18}O$	$^{87}Sr/^{86}Sr$
		wt%	wt%	wt%	wt%	wt%	wt%	wt%	wt%	wt%	wt%	ppm	ppm	ppm	ppm	ppm	ppm	‰	‰	
To-8	MIC	0.28	0.13	0.57	0.33	0.52	54.72	n.d.	0.02	0.01	43.30	40	23	19	156	27	3	1.97	28.96	0.70740
To-9	MAC	0.28	0.12	0.85	0.30	0.60	54.70	0.08	0.08	n.d.	42.89	40	28	22	168	12	5	2.10	29.30	
To-9A	MIC	0.06	0.08	0.22	0.09	0.83	54.62	0.21	0.09	n.d.	43.73	30	19	13	164	20	n.d.	2.06	28.97	
To-11	MAC	n.d.	0.11	0.60	0.18	0.64	55.01	0.07	n.d.	0.01	43.27	42	32	14	143	17	n.d.	1.81	28.95	
To-16	MIC	n.d.	0.11	0.70	0.29	0.63	56.04	0.07	n.d.	0.02	42.04	39	25	9	214	11	n.d.	1.69	28.71	
To-21	TRS	9.64	0.16	2.42	0.74	0.97	45.19	0.08	0.58	0.03	40.09	33	15	15	269	12	n.d.	2.09	28.74	

MIC = microcrystalline; MAC = macrocrystalline; TRS = traslucid; n.d. = not detected.

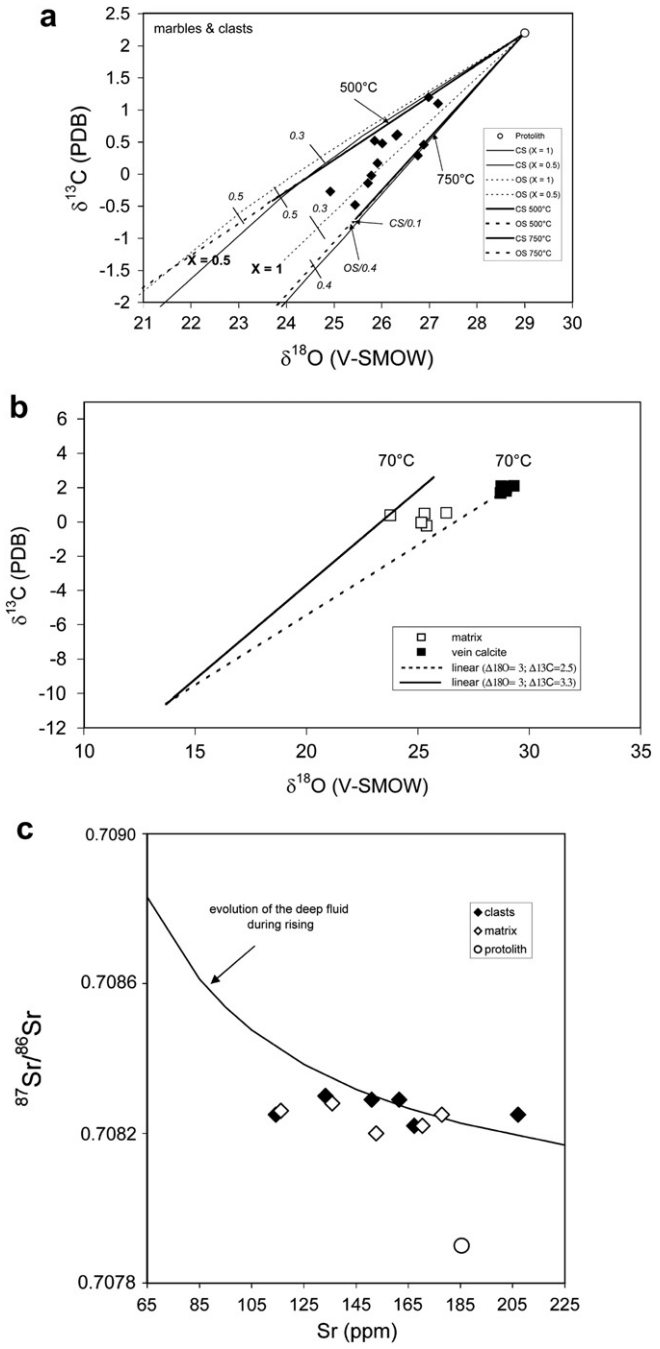

Fig. 9. (a) Modeling of the isotopic effects on damaged marble and the marble clasts in the fault core due to thermal decomposition of marble protolith under closed system (heavy lines) and open system (heavy dotted lines) conditions at temperatures of 500 and 750 °C. CS/0.1 and CO/0.4 arrows point to the isotopic composition of the residual marble after 90% and 60% decomposition took place in closed system and open system, respectively. See text for references on the governing equations and the CO_2–$CaCO_3$ carbon and oxygen isotope fractionation factors. The decomposition isotopic effects are compared with those due to fluid-marble protolith interaction in closed system (light solid line) and open system (light dotted line) at 70 °C and bicarbonate mole fractions X_{HCO_3} of 0.5 and 0.8 in the fluid, as described by the integrated form of a mass balance equation. Small bold bars and italicized numbers indicate the water–rock interaction progress in terms of ratio between the atom percentage of oxygen in water and the atom percent of oxygen in rock See text for references on the governing equations and carbon and oxygen isotope fractionation factors of the $CaCO_3$–HCO_3–H_2O system; (b) Mass balance modeling of the isotopic composition of matrix and vein calcite assuming they crystallized from a fluid after interaction with host marble at 70 °C and varying water to rock ratios. See text for references on the governing equations and the isotope fractionation factors of the $CaCO_3$–HCO_3–H_2O system, and the parameters used in the simulation; (c) Relation between $^{87}Sr/^{86}Sr$ and Sr in marble (massive and damaged), marble clasts and matrix calcite samples. The curve depicts the evolution of a fluid rising from the Paleozoic basement and leaching additional Sr from the rocks through which the fluid passed, i.e. Carrara marble and underlying carbonate formations. See text for applied chemical and isotopic constraints.

used for calculating the isotopic composition of precipitated calcite from the final fluid after exchange equilibrium with marble (calcite), assuming bicarbonate as the dominant form of dissolved carbon, are:

$$\delta^{13}C_{cal} = \delta^{13}C^{i}_{HCO_3} + 10^3 \ln \alpha^{cal}_{HCO_3} + (R/W)\Delta^{13}C^{i}_{f}$$

$$\delta^{18}O_{cal} = \delta^{18}O^{i}_{H_2O} + 10^3 \ln \alpha^{cal}_{H_2O} + (R/W)\Delta^{18}O^{i}_{f}$$

where i = initial composition, f = final composition, α = isotope fractionation factor (dependent on temperature) between calcite and bicarbonate or calcite and water, R/W = rock to water ratio in terms of atom percentage of carbon or oxygen in rock (R) and fluid (W), and $\Delta^{i}_{f} = \delta^{i}_{rock} - \delta^{f}_{rock}$. Assumptions in the calculations were a fluid temperature of 70 °C, initial $\delta^{13}C_{HCO3}$ of −12‰ and $\delta^{18}O_{H2O}$ of −7‰ in the fluid, isotope fractionation factors of 1.4‰ for carbon (calcite–bicarbonate) and 20.7‰ for oxygen (calcite–water), and Δ^{i}_{f} values in the range of 2.5–3.3 ‰ for carbon and 3 ‰ for oxygen isotopes. The obtained model accounts for the data distribution of matrix calcite samples in the $\delta^{13}C - \delta^{18}O$ space of Fig. 9b. Calculated $\delta^{18}O(H_2O)$ values in equilibrium with matrix calcite at 70 °C (O'Neil et al., 1969) range from +3.7 to +5.1‰, corresponding to W/R ratios of 0.23–0.31 in terms of atom percentage of carbon or oxygen in the fluid (W) and rock (R), i.e. 124–168 g H_2O/kg $CaCO_3$. The vein calcite data fit this model (Fig. 9b), that is they were deposited from a fluid of 70 °C and $\delta^{18}O(H_2O) = +8‰$, corresponding to a meteoric water with an initial $\delta^{18}O$ of −7‰ which interacted with marble under a W/R ratio of 0.20, corresponding to 110 g H_2O/kg $CaCO_3$. According to the metal concentrations (Fig. 8c), the vein depositing fluid should have been different than the matrix depositing one, and its source was probably local.

5.5. $^{87}Sr/^{86}Sr$ vs. Sr

The $^{87}Sr/^{86}Sr$ ratios of clasts and matrix samples from the cataclasite fault core can be explained by exchange and precipitation from a fluid rising, possibly, from the basement and enriched in Sr by dissolution of the carbonate host rocks. The fluid left the basement presumably carrying high radiogenic Sr (see Cortecci et al., 2003 for the chemical composition of basement siliciclastic metamorphic rocks), and acquired additional low radiogenic Sr during ascendance from the carbonate rock units. The evolution model shown in Fig. 9c assumes an initial Sr concentration in the fluid of 5 mg/L with a $^{87}Sr/^{86}Sr$ ratio of 0.72 (e.g. Faure, 1986), and a $^{87}Sr/^{86}Sr$ ratio of 0.70790 for marble protolith (Table 1, and Cortecci et al., 2003). The latter $^{87}Sr/^{86}Sr$ ratio is nearly equal to the mean ratio of 0.70793 measured for Sr in the calcite fraction of the carbonate rocks underlying the Carrara marble (Cortecci et al., 1999). All values show a good fit to the model implying that the calcite-solution distribution coefficient for Sr was close to a unit value during the precipitation of secondary calcite in the clasts and matrix. Consequently, the solid phase acquired the Sr concentration of the solution. This anomalously high distribution coefficient can be justified with the very fine size of the matrix calcite, as well as with the inferred temperature of deposition (Land, 1980).

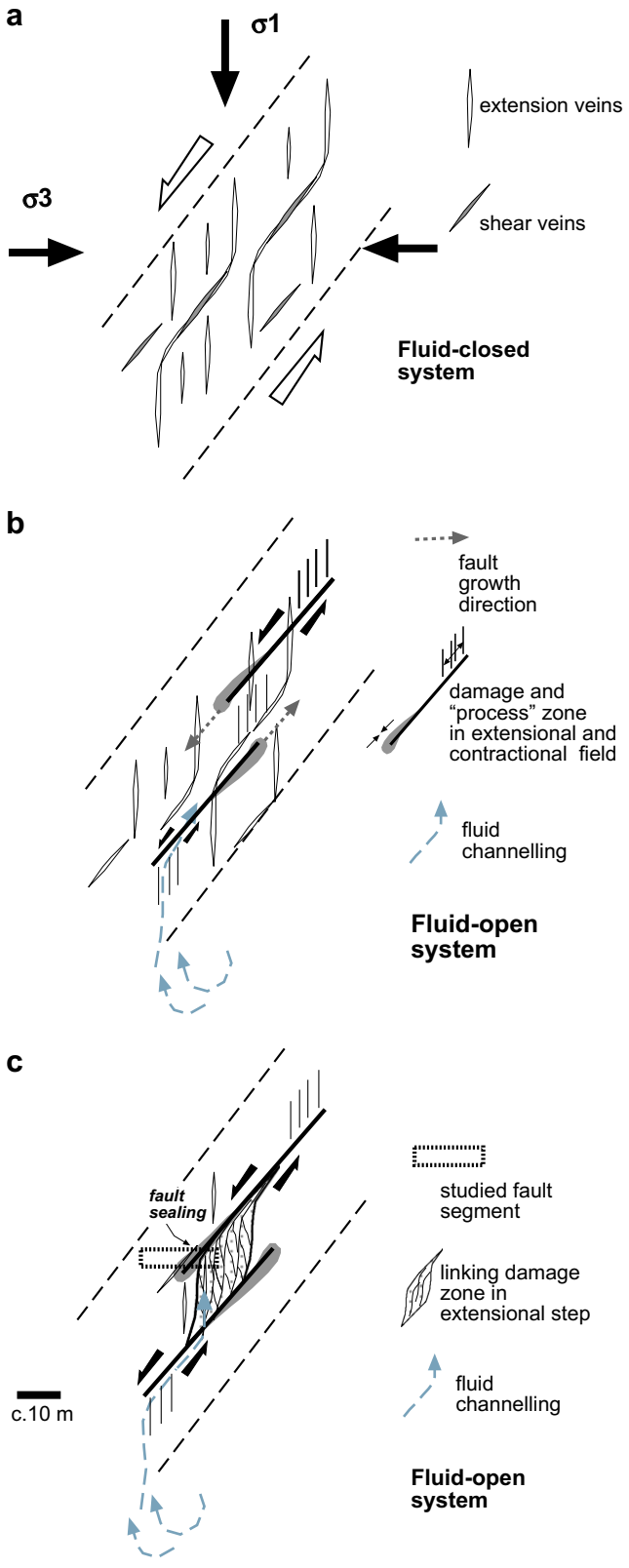

Fig. 10. Sketch model for structural evolution and fluid behaviour of the fault studied. a) Early stage of deformation with development of extensional and shear veins in a locally closed fluid system; b) evolution of deformation within an open fluid system. In this stage localization of faulting could have occurred in coarse grained qz–calcite shear veins, as documented by relicts vein within the fault core. Damage zone fracturing, characterizing extensional field give way to horse-tail like splays, following (?) some precursory early stage of distributed crystal-plastic deformation better developed in contractional field ("ductile" bead) at fault tip; (c) sealing of the hangingwall domain, fluid channelling and linking-damage zone at a releasing extensional step near a fault tip could be finally related to the observed deformation pattern.

6. Overall discussion and conclusion

6.1. Fault zone architecture

The studied normal fault shows what we infer to be a heterogeneous strain distribution between the hangingwall and the footwall. In part, this strain is marked by a variety of structures present in a well defined fault core and in an asymmetric damage zone that is basically confined to only the footwall. This contrasts, all of the normal fault-related asymmetric damage zones described in the literature (Berg and Skar, 2005 and references), with the exception of Doughty (2003), which show a wider hangingwall damage zone. As suggested by Knott et al. (1996), however, damage zone width can be related to a fault throw and strain variation in the rock volume around the master fault. The damage zone widens with increasing fault throw and is widest in the tensile field of a normal fault which can be in the hangingwall or the footwall depending on the specific observed segment of the larger fault.

The asymmetry of strain across a normal fault could be related to several factors (Berg and Skar, 2005) such as: host, layer thickness of the protolith (e.g. bedding), irregularities along the fault surface, displacement and relative proximity to the inclined fault core. In our case the effects of lithology and layer thickness can be considered as non-relevant because the host rock is basically the same in hangingwall and footwall blocks and the layers are missing. Both domains contain marbles with the same metamorphic and structural history as evident at the microscopic scale by the calcite microfabric. Mechanical properties of the hangingwall and footwall can be therefore considered the same at the time of faulting. Consequently, irregularities of the fault trace, displacement and growth process of the fault zone have to be invoked to explain the observed architectural features of the fault zone as illustrated below.

6.2. Microstructural features

The observed microstructures in the damage zone, in the cataclasite clasts and in particular within the rimming fault core bounding upper slip surface (mechanical twinning, sutured grain and twin boundaries, a second generation of recrystallized fine grained calcite at the border of larger original coarse calcite grains) testify the activity of crystal-plasticity and incipient dynamic recrystallization through grain boundary migration and bulge nucleation. The observed meso- and microstructural features, therefore, suggest alternating brittle and crystal-plastic deformation during accommodation of strain around the fault. This is not surprising since there has been documentation in the more recent literature of widespread coexistence of macroscopically brittle (cataclastic) and microscopically "ductile" (mylonitic) structures in natural carbonate deformation (e.g. Kennedy and Logan, 1997; Kirschner and Kennedy, 2001; Badertscher and Burkhard, 2001; Kennedy and White, 2001; Liu et al., 2002). Experimental deformation studies documented twin boundary migration recrystallization in fine grained, synthetic hot-pressed calcite (Rutter, 1995) and, for Carrara marble, bulge nucleation in low-temperature, high shear strain torsion experiments (Barnhoorn et al., 2000). Moreover Fredrich et al. (1989), in the investigation of the brittle to plastic transition in Carrara marble, reproduced microstructural features similar to those we found in thin sections. Fredrich et al. (1989) indicate that in the semi-brittle regime, deformation mechanisms including microcracking, twinning and dislocation glide can interact in a variety of ways. What is interesting is that the activation of crystal-plasticity in localized domains of a fault zone

can result in porosity reduction, low permeability and fluid localization e.g. the formation of a seal (Kennedy and White, 2001). This point will be further discussed later on.

6.3. Fluid–rock interaction

The results of the chemical and isotopic analyses indicate that fluids were involved in the development of the fault zone and localization of deformation.

Compared to the protolith, the fault damage zone and core are depleted in ^{13}C and ^{18}O, and are enriched in ^{87}Sr and base metals. The source of base metals and radiogenic ^{87}Sr may be located in the underlying Paleozoic basement with some contribution from carbonate formations (Grezzoni and Marmi Dolomitici fms.) interposed between the basement and Carrara marbles. Evidence for this inference includes:

(1) Mn and Fe concentrations in calcite from the fault core matrix are among the highest in the sample set and appear to be genetically related, and their provenance can be found in the siliciclastic basement, and (2) fluids, possibly of meteoric origin, interacted with the fault zone, after rising from the basement. These metamorphic basement rocks have a characteristic geochemical signature being rich in Fe, Mn and base metals compared with the marble. This type of exotic fluid infiltrated after a first phase of deformation in which extensional and shear veins developed in a closed system. Based on geochemical modeling, water–rock interaction and calcite deposition should have been nearly synchronous, and possibly took place at 70 °C. Both events may have occurred at about 3 km depth (25 °C/km geothermal gradient), in keeping with geological data on the underground position of the Carrara marbles at the time of deformation (Fellin et al., 2007; Molli, 2008). Fig. 10 shows a sketch model for the structural evolution and fluid interaction of the high angle normal fault studied. The early stage of deformation (Fig. 10a) can be associated with extensional and shear veins now observable in both hangingwall and footwall blocks as part of the deformation zone developed at decameter-scale. From geochemical data we infer an initial, locally closed system where a "stationary" fluid phase migrates over only meter scale distances. During a second stage of development, the system (Fig. 10b) is characterized by localization of the deformation possibly in precursory coarse grained calcite/quartz shear veins of stage 1. These are observable near the main upper slip surface as well as in relicts affected by cataclastic deformation within the fault core. During this second stage, a "process zone" (Engelder, 1974; Knipe and Lloyd, 1994; Vermilye and Scholz, 1998) of crystal-plastic deformation possibly developed at the head ("ductile bead" of Elliott, 1976) of the fracture and accommodates fault tip distortions in the contractional field similar to a mode-II geometry of crack propagation (Atkinson, 1987; Vermilye and Scholz, 1998; Kim et al., 2004). Pervasive fracturing characterizes the extensional field giving way to horse-tail like splays. An extensional relay-step (Peacock et al., 2000) domain between two segments of the fault produced the geometrical irregularity of fault and the linking-damage zone in which fluids localize deformation. During this second stage, basement-derived fluids channelized within fault zone leading to significant geochemical alteration in the protolith with depletion of ^{13}C and ^{18}O, and enrichment in base metals and ^{87}Sr. As evolution of the second stage (Fig. 10c) progressed, displacement of the main upper slip surface may have caused sealing of the hangingwall domain by localized calcite crystal-plasticity and confined fluids in the footwall of a propagating fault tip. The resulting final geometry of the deformation pattern can be therefore controlled by a process associated with a linking-damage zone at a fault tip, development of fault core, localization and channelling of fluids through it in a transiently open fluid system. Finally, we suggest that syn-kinematic local microstructural modification of calcite microfabric possibly played an important role in confining fluid percolation.

Acknowledgements

S. Caine, J.C. White, T. Blenkinshop, F. Agosta and E. Tondi are thanked for their very detailed and useful comments which improved the original submitted manuscript. Ing. Maura Pellegri and all the staff of the Unità operativa Ingegneria Mineraria Azienda U.S.L. n°1 Massa-Carrara, are thanked for support and discussions. This work was supported by PRIN 2005, Pisa University and CNR funds.

References

Abbate, E., Balestrieri, M.L., Bigazzi, G., Norelli, P., Quercioli, C., 1994. Fission-track dating and recent rapid denudation in Northern Apennines, Italy. Memorie Società Geologica Italiana 48, 579–585.

Agosta, F., Aydin, A., 2006. Architecture and deformation mechanism of a basin-bounding normal fault in Mesozoic platform carbonates, central Italy. Journal of Structural Geology 28, 1445–1467.

Agosta, F., Prasad, M., Aydin, A., 2007. Physical properties of carbonate fault rocks, Fucino basin (Central Italy): implications for fault seal in platform carbonates. Geofluids 7, 19–32.

Atkinson, B.K., 1987. Fracture Mechanics of Rocks. Academic Press, London.

Antonellini, M., Aydin, A., 1994. Effect of faulting on fluid flow in porous sandstones: petrophysical properties. AAPG Bulletin 78, 355–377.

Badertscher, N.P., Burkhard, M., 2001. Brittle–ductile deformation in the Glarus thrust Lochseiten (LK) calc-mylonite. Terra Nova 12, 281–288.

Balestrieri, M.L., Bernet, M., Brandon, M.T., Picotti, V., Reiners, P., Zattin, M., 2003. Pliocene and Pleistocene exhumation and uplift of two key areas of the Northern Apennines. Quaternary International 101–102, 67–73.

Barnhoorn, A., Kunze, K., Bystricky, M., Burlini, L., 2000. Microstructural evolution of Carrara marble deformed to high strains torsion. Eos (Transactions, American Geophysical Union) 81, 1122.

Berg, S.S., Skar, T., 2005. Controls on damage zone asymmetry of a normal fault zone: outcrop analyses of a segment of the Moab Fault, SE Utah. Journal of Structural Geology 27, 1803–1822.

Billi, A., Salvini, F., Storti, F., 2003. The damage zone-fault core transition in carbonate rocks: implications for fault growth, structure and permeability. Journal of Structural Geology 25, 1779–1794.

Blenkinshop, T.G., 1989. Thickness–displacement relationships for deformation zones: discussion. Journal of Structural Geology 11, 1051–1054.

Blenkinshop, T.G., Rutter, E.H., 1986. Cataclastic deformation of quartzite in the Moine thrust zone. Journal of Structural Geology 8, 669–681.

Brodie, K.H., Rutter, E., 1985. On the relationship between deformation and metamorphism, with special reference to the behaviour of basic rocks. In: Thompson, A.B., Rubie, D.C. (Eds.), Kinetics, Textures and Deformation, Advance in Physical Geochemistry, vol. 4. Springer, New York, pp. 138–179.

Bruhn, R.L., Parry, W.T., Yonkee, W.A., Thompson, T., 1994. Fracturing and hydrothermal alteration in normal fault zones. Pure and Applied Geophysics 142, 609–642.

Burlini, L., Bruhn, D., 2005. High-strain zones: laboratory perspective on strain softening during ductile deformation. In: Bruhn, D., Burlini, L. (Eds.), Structure and Physical Properties. Geological Society of London, Special Publication, vol. 245, pp. 1–24.

Caine, J.S., Evans, J.P., Forster, C.B., 1996. Fault zone architecture and permeability structure. Geology 24, 1025–1028.

Caine, J.S., Forster, C.B., 1999. Fault zone architecture and fluid flow: insights from field data and numerical modeling. In: Haneberg, W.C., Mozley, P.S., Moore, J.C., Goodwin, L.B. (Eds.), Faults and Sub-surface Fluid Flow in the Shallow Crust. American Geophysical Union Geophysical Monograph, vol. 113, pp. 101–127.

Caine, J.S., Tomusiak, S.R.A., 2003. Brittle structures and their role in controlling porosity and permeability in a complex Precambrian crystalline-rock aquifer system in the Colorado Rocky Mountain Front Range. Geological Society of America Bulletin 115, 1410–1424.

Carmignani, L., Kligfield, R., 1990. Crustal extension in the northern Apennines: the transition from compression to extension in the Alpi Apuane core complex. Tectonics 9, 1275–1303.

Carmignani, L., Decandia, F.A., Disperati, L., Fantozzi, P.L., Lazzarotto, A., Liotta, D., Kligfield, R., Meccheri, M., 2000. Inner northern Apennines. In: Martini, P., Vai, G.B. (Eds.), Anatomy of an Orogen: the Apennines and Adjacent Mediterranean Basins. Kluwer Academic Publisher, Dordrecht, pp. 197–214.

Cello, G., Invernizzi, C., Mazzoli, S., Tondi, E., 2001a. Fault properties and fluid flow patterns from Quaternary faults in the Apennines, Italy. Tectonophysics 336, 63–78.

Cello, G., Tondi, E., Micarelli, L., Invernizzi, C., 2001b. Fault zone fabrics and geofluid properties as indicators of rock deformation modes. Journal of Geodynamics 32, 543–565.

Chacko, T., Mayeda, T.K., Clayton, R.N., Goldsmith, J.R., 1991. Oxygen and carbon isotope fractionation between CO_2 and calcite. Geochimica et Cosmochimica Acta 55, 2867–2882.

Chester, F.M., Logan, J.M., 1986. Implications for mechanical properties of brittle faults from observations of the Punchbowl fault zone, California. Pure and Applied Geophysics 124, 79–106.
Cortecci, G., Dinelli, E., Indrizzi, M.C., Susini, C., Adorni Braccesi, A., 1999. The Apuane Alps metamorphic complex, northern Tuscany: chemical and isotopic features of Grezzoni and Marmi Dolomitici. Atti Società Toscana Scienze Naturali Memorie, Serie A 106, 79–89.
Cortecci, G., Dinelli, E., Molli, G., Ottria, G., 2003. Geochemical evidence for fluid–rock interaction along high angle faults in the Alpi Apuane, NW Tuscany, Italy. Periodico Mineralogia 72, 35–47.
Doughty, P.T., 2003. Clay smear seals and fault sealing potential of an exhumed growth fault, Rio Grande Rift, New Mexico. AAPG Bulletin 87, 427–444.
Elliott, D., 1976. The energy balance and deformation mechanisms of thrust sheets. Proceedings Royal Society London A283, 289–312.
Elter, P., 1975. Introduction à la géologie de l'Apennin septentrional. Bulletin Société Géologique France 7, 956–962.
Engelder, J.T., 1974. Cataclasis and the generation of fault gouge. Geological Society of America Bulletin 85, 1515–1522.
Evans, J.P., 1990. Thickness–displacement relationships for fault zones. Journal of Structural Geology 12, 1061–1065.
Evans, J.P., Forster, C.B., Goddard, J.V., 1997. Permeability of fault-related rocks, and implications for hydraulic structure of fault zones. Journal of Structural Geology 19, 1393–1404.
Faulkner, D.R., Rutter, E.H., 2001. Can the maintenance of overpressured fluids in large strike-slip fault zones explain their apparent weakness? Geology 29, 503–506.
Faulkner, D.R., Lewis, A.C., Rutter, E.H., 2003. On the internal structure and mechanics of large strike-slip fault zone: field observations of the Carboneras fault in southeastern Spain. Tectonophysics 367, 235–251.
Faure, G., 1986. Principles of Isotope Geology, second ed. Wiley, New York.
Fellin, M.G., Reiners, P.W., Brandon, M.T., Wuthrich, E., Balestrieri, M.L., Molli, G., 2007. Thermochronologic evidence for exhumational history of the Alpi Apuane metamorphic core complex, northern Apennines, Italy. Tectonics 26, TC6015. doi:10.1029/2006TC002085.
Flodin, E., Aydin, A., 2004. Faults with asymmetric damage zones in sandstone, valley of Fire State Park, southern Nevada. Journal of Structural Geology 26, 983–988.
Fredrich, J.T., Evans, B., Wong, T.-F., 1989. Micromechanics of brittle to plastic transition in Carrara marble. Journal of Geophysical Research 94, 4129–4145.
Gat, J.R., 1981. Groundwater. In: Gat, J.R., Gonfiantini, R. (Eds.), The Water Cycle. Stable Isotope Hydrology–Deuterium and Oxygen-18, vol. 210. IAEA, Vienna, pp. 223–240. Technical report Series.
Han, R., Shimamoto, T., Hirose, T., Ree, J., Ando, J.-I., 2007. Ultraslow friction of carbonate faults caused by thermal decomposition. Science 316, 878–881.
Herz, N., Dean, N.E., 1986. Stable isotopes and archaeological geology: the Carrara marble, northern Italy. Applied Geochemistry 1, 139–151.
Hull, J., 1988. Thickness–displacement relationships for deformation zones. Journal of Structural Geology 10, 431–435.
Kennedy, L., Logan, J.M., 1997. The role of veining and dissolution in the evolution of fine-grained mylonites – the McConnel thrust. Journal of Structural Geology 19, 785–797.
Kennedy, L., White, J.C., 2001. Low-temperature recrystallization in calcite: mechanisms and consequences. Geology 29, 1027–1030.
Kim, Y.-S., Peacock, D.C.P., Sanderson, D.J., 2004. Fault damage zones. Journal of Structural Geology 26, 503–517.
Kim, Y.-S., Sanderson, D.J., 2005. The relationship between displacement and length of faults: a review. Earth Science Reviews 68, 317–334.
Kirschner, D.L., Kennedy, L., 2001. Limited syntectonic fluid flow in carbonate-hosted thrust faults of the Front Ranges, Canadian Rockyes, inferred from stable isotope data and structures. Journal of Geophysical Research 106, 8827–8840.
Knipe, R.J., 1993. The influence of fault zone processes and diagenesis on fluid flow. In: Horbury, A.D., Robinson, A.G. (Eds.), Diagenesis and Basin Development. American Association of Petroleum Geologists Studies in Geology, vol. 36, pp. 135–151.
Knipe, R.J., Lloyd, G.E., 1994. Microstructural analysis of faulting in quartzite, Assynt NW Scotland: implications for fault zone evolution. Pure and Applied Geophysics 143, 231–254.
Knott, S.D., Beach, A., Brockbank, P.J., Brown, J.L., McCallum, J.E., Welbon, A.I., 1996. Spatial and mechanical controls on normal fault populations. Journal of Structural Geology 18, 359–372.
Land, L.S., 1980. The isotopic and trace element geochemistry of dolomite: the state of the art. Society of Economic Paleontologists and Mineralogists 28, 87–110. Spec. Pub.
Labaume, P., Carrio-Schaffhauser, E., Gamond, J.-F., Renard, F., 2004. Deformation mechanisms and fluid-driven mass transfers in the recent fault zones of the Corinth Rift (Greece). Comptes Rendus Geoscience 336, 375–383.
Liu, J., Walter, J.M., Weber, K., 2002. Fluid-enhanced low-temperature plasticity of calcite marble: microstructures and mechanisms. Geology 30, 787–790.
Mandl, G., 2000. Faulting in Brittle Rocks. An Introduction to the Mechanics of Tectonic Faults. Springer, Berlin.
Mancktelow, N.S., Pennacchioni, G., 2005. The control of precursor brittle fracture and fluid–rock interaction on the development of single and paired ductile shear zones. Journal of Structural Geology 27, 645–661.
Marquer, D., Burkhard, M., 1992. Fluid circulation, progressive deformation and mass-transfer process in the upper crust: the example of basement–cover relationships in the External Crystalline Massifs, Switzerland. Journal of Structural Geology 14, 1047–1057.
McCrea, J.M., 1950. On the isotopic chemistry of carbonates and a paleotemperature scale. Journal Chemistry Physics 18, 849–857.
McCaig, A.M., 1988. Deep fluid circulation in fault zones. Geology 16, 867–870.
McGrath, A., Davison, I., 1995. Damage zone geometry around fault tips. Journal of Structural Geology 17, 1011–1024.
Meccheri, M., Molli, G., Conti, P., Blasi, P., Vaselli, L., 2007. The Carrara marbles (Alpi Apuane, Italy): a geological and economical updated review. Zeitschrift Deutschen Gesellschaft Geowissenschfaten 158, 719–735.
Micarelli, L., Benedicto, A., Wibberley, C.A.J., 2006. Structural evolution and permeability of normal fault zones in highly porous carbonate rocks. Journal of Structural Geology 28, 1214–1227.
Micklethwaite, S., Cox, S.F., 2004. Fault-segment rupture, aftershock-zone fluid flow, and mineralization. Geology 32, 813–816.
Miller, J.A., Viola, G., Mancktelow, N.S., 2008. Oxygen, carbon and strontium isotope constraints on the mechanisms of nappe emplacement and fluid rock interaction along the subhorizontal Naukulft Thrust, central Namibia. Journal of Geological Society 165, 739–753.
Molli, G., 2008. Northern Apennine–Corsica orogenic system: an updated overview. In: Siegesmund, S., Fugenschuh, B., Froitzheim, N. (Eds.), Tectonic Aspects of the Alpine–Dinaride–Carpathian System. Geological Society of London, Special Publications, vol. 298, pp. 413–442.
Molli, G., Vaselli, L., 2006. Structures, interference patterns, and strain regime during midcrustal deformation in the Alpi Apuane (Northern Apennines, Italy). Geological Society of America 414 (5), 79–93. Special Paper.
Molli, G., Heilbronner, R., 1999. Microstructures associated with static and dynamic recrystallization of Carrara marble (Alpi Apuane, NW Tuscany, Italy). Geologie en Mijnbouw 78, 119–126.
Molli, G., Conti, P., Giorgetti, G., Meccheri, M., Oesterling, N., 2000. Microfabric studies on the deformational and thermal history of the Alpi Apuane marbles (Carrara marbles), Italy. Journal of Structural Geology 22, 1809–1825.
Mussi, M., Leone, G., Nardi, I., 1998. Isotopic geochemistry of natural waters from the Alpi Apuane-Garfagnana area, northern Tuscany, Italy. Mineralogica et Petrographica Acta 41, 163–178.
Ohomoto, H., Rye, R.O., 1979. Isotopes of sulfur and Carbon. In: Barnes, H.L. (Ed.), Geochemistry of hydrothermal ore deposits, second ed. Wiley, New York, pp. 509–567.
O'Neil, J.R., Clayton, R.N., Mayeda, T.K., 1969. Oxygen isotope fractionation in divalent metal carbonates. Journal of Chemical Physics 51, 5547–5558.
Ottria, G., Molli, G., 2000. Superimposed brittle structures in the late orogenic extension of the northern Apennine: results from Carrara area (Alpi Apuane, NW Tuscany). Terra Nova 12, 1–8.
Patacca, E., Sartori, R., Scandone, P., 1992. Tyrrhenian basin and Apenninic arcs: kinematic relationships since Late Tortonian times. Memorie della Società Geologica Italiana 45, 425–451.
Peacock, D.C.P., 2002. Propagation, interaction and linkage in normal fault systems. Earth Science Reviews 58, 121–142.
Peacock, D.C.P., Knipe, R.J., Sanderson, D.J., 2000. Glossary of normal faults. Journal of Structural Geology 22, 291–305.
Rawling, G.C., Goodwin, L.B., Wilson, J.L., 2001. Internal architecture, permeability structure, and hydrologic significance of contrasting fault-zone types. Geology 29, 43–46.
Rutter, E.H., 1972. The influence of interstitial water on the rheological behaviour of calcite rocks. Tectonophysics 14, 13–33.
Rutter, E.H., 1995. Experimental study of the influence of stress, temperature, and strain on the dynamic recrystallization of Carrara marble. Journal of Geophysical Research 100, 24.651–24.663.
Schmid, S.M., Paterson, M.S., Boland, J.N., 1980. High temperature flow and dynamic recrystallization in Carrara marble. Tectonophysics 65, 245–280.
Schultz, S.E., Evans, J.P., 1998. Spatial variability in microscopic deformation and composition of the Punchbowl fault, southern California: implications for mechanisms, fluid–rock interaction, and fault morphology. Tectonophysics 295, 223–244.
Shieh, Y.N., Taylor, H.P., 1969. Carbon and hydrogen isotope studies at contact metamorphism in the Santa Rosa Range, Nevada and other areas. Contribution Mineralogy Petrology 20, 306–356.
Sibson, R.H., 1977. Fault rocks and fault mechanism. Journal of the Geological Society London 133, 191–213.
Sibson, R.H., 1992. Implications of fault-valve behaviour for rupture nucleation and recurrence. Tectonophysics 211, 283–293.
Sibson, R.H., 1996. Structural permeability on fluid-driven fault-fracture meshes. Journal of Structural Geology 18, 1031–1042.
Storti, F., Billi, A., Salvini, F., 2003. Particle size distribution in natural carbonate fault rocks: insights for non-self similar cataclasis. Earth and Planetary Science Letters 206, 173–186.
Taylor, B.E., 1986. Magmatic volatiles: isotopic variation of C, H and S. In: Valley, I.W., Taylor, H.P., O'Neil, J.R. (Eds.), Stable Isotopes in High Temperature Geological Processes. Reviews in Mineralogy, vol. 16, pp. 185–225.
Vermilye, J.M., Scholz, C.H., 1998. The process zone: a microstructural view. Journal of Geophysical Research 103, 12223–12237.
Vogel, J.C., Ehhalt, D., 1963. The Use of Carbon Isotopes in Groundwater Studies. Radioisotopes in Hydrology. IAEA, Vienna, pp. 383–395.
Watterson, J., 1986. Fault dimensions, displacements and growth. Pure and Applied Geophysics 124, 365–373.
Zheng, Y.F., Hoefs, J., 1993. Carbon and oxygen isotopic covariations in hydrothermal calcites. Mineralium Deposita 28, 79–89.